

Research Article

GPS/Low-Cost IMU/Onboard Vehicle Sensors Integrated Land Vehicle Positioning System

Jianchen Gao, Mark G. Petovello, and M. Elizabeth Cannon

Position, Location, and Navigation (PLAN) Group, Department of Geomatics Engineering, University of Calgary, 2500 University Drive NW, Calgary, AB, Canada T2N 1N4

Received 14 October 2006; Accepted 9 April 2007

Recommended by Gunasekaran S. Seetharaman

This paper aims to develop a GPS, low-cost IMU, and onboard vehicle sensors integrated land vehicle positioning system at low cost and with high (cm level) accuracy. Using a centralized Kalman filter, the integration strategies and algorithms are discussed. A mechanism is proposed for detecting and alleviating the violation of the lateral nonholonomic constraint on the wheel speed sensors that is widely used in previous research. With post-mission and real-time tests, the benefits gained from onboard vehicle sensors and the side slip detection and alleviation mechanism in terms of the horizontal positioning accuracy are analyzed. It is illustrated by all the tests that GPS plays a dominant role in determining the absolute positioning accuracy of the system when GPS is fully available. The integration of onboard vehicle sensors can improve the horizontal positioning accuracy during GPS outages. With respect to GPS and low-cost IMU integrated system, the percentage improvements from the wheel speed sensor are 90.4% for the open-sky test and 56.0% for suburban area real-time test. By integrating all sensors to detect and alleviate the violation of the lateral nonholonomic constraint, the percentage improvements over GPS and low-cost IMU integrated system can be enhanced to 92.6% for open-sky test and 65.1% for the real-time test in suburban area.

Copyright © 2007 Jianchen Gao et al. This is an open access article distributed under the Creative Commons Attribution License, which permits unrestricted use, distribution, and reproduction in any medium, provided the original work is properly cited.

1. INTRODUCTION

In recent years, significant attention has been paid to intelligent vehicle systems. Among them are antilock brake systems (ABS), traction control (TC), vehicle stability control (VSC), vehicle safety control such as forward-collision avoidance, to name a few [1]. In these systems, numerous sensors are being employed, and the positioning accuracy and system redundancy have crucial impacts on their performance [2]. Due to the complementary features, GPS/INS integrated systems have been widely used for vehicular positioning and navigation [3–5]. With respect to GPS positioning, centimeter-level accuracies can be achieved by using carrier phase measurements in a double difference approach whereby the integer ambiguities are resolved correctly. However, difficulties arise during significant shading from obstacles such as buildings, overpasses, and trees. To bridge GPS gaps and reduce the INS error growth, many auxiliary sensors, such as compasses, inclinometers, tilt meters, and odometers have been used to provide further external aiding [6, 7]. Typically, the wheel speed sensors are fundamental components of an ABS which is standard equipment on nearly all vehicles [8]. Therefore the integration of the wheel speed sensor with GPS/INS has been extensively studied [9–11].

Since the wheel speed sensor can be used to estimate the vehicle's velocity in the forward direction, most of the previous research related to the integration of wheel speed sensor information with GPS/INS applied two nonholonomic constraints on the lateral and vertical directions. These nonholonomic constraints are effective only when the vehicle operates on a flat road and no side slip occurs [12, 13]. The nonholonomic constraints are no longer valid when the vehicle runs off road or on an icy or bumpy road where a larger side slip angle can occur. In a land vehicle positioning system, the violation of the nonholonomic constraints is always accompanied by larger side slip angles [13]. Side slip is a very complicated phenomenon associated with road conditions and high vehicle dynamics (e.g., fast driving, sharp turning as well as high pitch and roll angular rates). It is not easily modeled and estimated. Reference [14] investigated a model-based Kalman filter with GPS velocity measurements to estimate side slip. However, its estimation accuracy relies heavily on the correctness of the model.

As a commonly used system for a land vehicle positioning system, a GPS/INS integrated system harnesses either a tactical grade or low-cost IMU. The high cost of a tactical grade IMU constitutes its main limitation to commercial deployment. The performance of a low-cost IMU degrades quickly

over a short time interval of GPS outages. A larger error drift is not well suited to such a land vehicle positioning system that has a strict requirement on positioning accuracy as the intelligent or autonomous vehicle control system. To meet the requirement of the low-cost and high positioning accuracy for the land vehicle positioning system, a GPS receiver, low-cost IMU, and onboard vehicle sensors are integrated into a land vehicle positioning system. The onboard vehicle sensors come from the vehicle stability control system, including two horizontal G sensors (accelerometers) and yaw rate sensor (i.e., a two-dimensional automotive grade inertial unit) as well as wheel speed sensors. After describing the integration strategy, a mechanism is proposed for the computation of the side slip angle as well as the detection and compensation of the violation of the lateral nonholonomic constraint. The tests for the post-mission and the real-time were conducted. The benefits after integrating the onboard vehicle sensors and using the side slip detection mechanism in terms of the horizontal positioning accuracy are analyzed.

2. COORDINATE FRAME DEFINITIONS FOR ONBOARD VEHICLE SENSORS AND THE LOW-COST IMU

The MEMS low-cost IMU consists of three triads of accelerometers as well as three triads of gyros, which, respectively, measure three-dimensional specific forces and angular rates with respect to the IMU body frame. The low-cost IMU body frame represents the orientation of the IMU axes. The origin of the body frame is at the center of the IMU. The IMU axes are assumed to be approximately coincident with the moving platform upon which the IMU sensors are mounted with the Y-axis pointing towards the front, the X-axis pointing toward the right, and the Z-axis being orthogonal to the X and Y axes to complete a right-handed frame. The low-cost IMU is mechanized in ECEF (earth-centered earth-fixed) frame (e frame) herein although any convenient frame could be used.

The onboard vehicle sensors discussed in this paper include: two rear and two front wheel speed sensors, two G sensors, and a yaw rate sensor. The wheel speed sensors (WSS) are attached to the wheels of the vehicle and provide estimates of the forward velocity in vehicle frame that are susceptible to the change in actual rolling tire radius and the tire longitudinal slip. The vehicle frame is attached to the vehicle at its center of gravity to represent the orientation of the vehicle. The X-axis points towards the right side of the vehicle. The Y-axis points towards the forward direction of the vehicle. The Z-axis is orthogonal to the X and Y axes to complete a right-handed frame. The wheel speed sensor measurements are represented in the vehicle frame.

The G sensors and yaw rate sensor that are placed on the chassis of the vehicle actually constitute a two-dimensional automotive grade inertial unit. The G sensors measure the lateral and longitudinal specific forces, and the yaw rate sensor measures angular rate with respect to the vertical direction of the G sensors/yaw rate sensor unit (GL/YRS). The G

sensors and yaw rate sensor (GL/YRS) body frame follows the same definition of the low-cost IMU.

It is an ideal case that the IMU body frame coincides to the vehicle frame. However, due to installation “error” of the IMU, the bore sight of the IMU is misaligned with the vehicle frame in most cases. The tilt angles between the IMU body frame and the vehicle frame will result in some errors when the position or velocity is transformed from one frame to another without taking into account the tilt angles. As such, a calibration algorithm for estimating the tilt angles between the IMU body frame and the vehicle frame is implemented in this paper.

For simplicity, the low-cost IMU and the GL/YRS unit body frames, however, are assumed to be aligned despite tilt angles that may actually exist between these two frames. Theoretically, the tilt angles will lead to constant biases of the accelerometer measurements [15]. In the land vehicle positioning system with a relatively small attitude change rate, this assumption holds in most cases with the biases of IMU and GL/YRS measurements being estimated by the Kalman filter.

3. GPS/LOW-COST IMU/ONBOARD VEHICLE SENSOR INTEGRATION STRATEGY

Figure 1 describes the GPS, low-cost IMU, WSS and GL/YRS integration strategy, which consists of two basic modules, GPS/INS/WSS and GPS/INS/GL/YRS as well as a combined module of GPS/INS/WSS/GL/YRS. All available sensor measurements are combined using a tight coupling strategy at each epoch to obtain a globally optimal solution using one centralized Kalman filter [16]. For the equipment used, the IMU data rate is 100 Hz, and its mechanization equation output rate is set to 10 Hz. The GPS measurements used herein are double-differenced carrier phase, double-differenced Doppler, and double-differenced pseudorange at a 1 Hz rate. The onboard vehicle sensors are sampled at 100 Hz. To make a tradeoff between the system accuracy and the computational load in the real-time test, the vehicle sensor data are thinned to 1 Hz for the update of the centralized Kalman filter. The position, velocity, and attitude information of the integrated system are given by implementing the mechanization equation of the low-cost MEMS IMU in ECEF frame.

Due to the centralized processing approach, the satellite measurements are estimated by using the integrated position and velocity. The raw GPS measurements and the estimated satellite measurements are compared to derive the GPS measurement misclosures in the centralized Kalman filter. When the ambiguities need to be fixed, the float double differenced ambiguities are added to the state vector and estimated in the centralized Kalman filter. The integer ambiguities are resolved using the LAMBDA [17] method with the real-valued ambiguities and their corresponding estimated covariance matrix from the Kalman filter.

The forward-direction velocity in the vehicle frame can be determined from the WSS, while two nonholonomic constraints are applied to the vertical and lateral directions of the

vehicle frame. The wheel speed sensor provides the absolute velocity information to update the centralized Kalman filter. During GPS outages, the nonholonomic constraints, as well as the absolute velocity information, can constrain the velocity and consequently the position drift of the stand-alone INS system.

The nonholonomic constraints imply that the vehicle does not move in the vertical or the lateral directions. The nonholonomic constraints hold only when the vehicle runs on flat road with small side slip. On the bumpy road with a larger side slip, the assumption of nonholonomic constraints is no longer valid.

The wheel speed sensors used in this research are of the passive type. The number of pulses per rotation is measured with the sensor teeth going through a passive magnetic field. The wheel speed is consequently correlated with the number pulses per rotation as well as the radius of the wheel tire. In practical use, the tire size is sensitive to many factors such as a payload, the driving conditions, temperature, air pressure, and the tread wear. Additionally, the IMU body frame does not always coincide with the vehicle frame. Thus, the scale factor of the wheel speed sensor and the tilt angles between the vehicle and body frames are augmented into the state vector of the centralized Kalman filter, as described in Figure 1.

Instead of providing the absolute velocity as the WSS does, the GL/YRS unit derives the lateral and longitudinal velocity with the initial velocity being provided from the integrated system. GL/YRS unit performs a velocity update in its body frame by computing the measurement misclosures (also termed as “innovations”) between the integrated velocity (being transformed from ECEF frame into the body frame) and lateral/longitudinal velocity computed from GL/YRS. Similarly to the low-cost MEMS IMU, the biases of the G sensors and yaw rate sensor are augmented into the state vector of the centralized Kalman filter.

As illustrated in Figure 1, the centralized Kalman filter is a closed loop type. It indicates that the relationship between the centralized Kalman filter and the velocity update from either wheel speed sensor or GL/YRS unit are bidirectional. In one way, the GPS update provides an external aiding to limit the INS drift error when GPS is available. During GPS outages, WSS and GL/YRS will continue to update the centralized Kalman filter and bridge GPS data gap. In another way, the estimated error states feedback to the integrated solutions as well as the low-cost IMU, WSS, and GL/YRS measurements. With the feedback information, the integrated position, velocity, and the attitude angles can be corrected by the estimated error states of position, velocity, and the misalignment angles. Also, the estimated accelerometer and gyro biases, WSS scale factor and GL/YRS biases can rectify the IMU and onboard vehicle sensor measurements, respectively.

It has been verified by [11] that the WSS with two nonholonomic constraints can significantly improve the positioning accuracy during GPS outages. The lateral nonholonomic constraint is very close to a real condition with a small side slip, and it is violated with a larger side slip. This constitutes a weak point of GPS/INS/WSS integration module.

The quality of automotive grade GL/YRS is similar to that of the low-cost IMU. Thus, its error will drift at the same rate as the low-cost IMU during GPS outages, and the improvement on the positioning accuracy gained from GL/YRS is less significant than from WSS.

Based on the above analysis, Figure 2 describes this interactive relationship between WSS and GL/YRS. The absolute velocity update from the WSS measurements limits the longitudinal velocity drift error. Consequently, the accuracy of the initial longitudinal velocity for GL/YRS is increased. On another hand, the side slip angle can be calculated from the lateral and longitudinal velocities. The side slip angle information provides a way to detect and alleviate the violation of the lateral nonholonomic constraint. When the side slip angle is smaller than a threshold, it means that the lateral constraint is most likely valid. However, when the side slip angle goes beyond a specific threshold, it indicates that the lateral nonholonomic constraint is violated. To compensate the violation of the lateral nonholonomic constraints, one possible way is to make use of the lateral velocity calculated from the GL/YRS to replace the lateral nonholonomic constraint as will be discussed later.

4. INTEGRATION ALGORITHMS

The development of the integration algorithms includes the derivations of the dynamic and measurement models used in the Kalman filter, as well as the computation of side slip angle, and the mechanism for detecting and alleviating the violation of the nonholonomic constraints used in GPS/INS/WSS/GL/YRS integration strategy.

The error states estimated by GPS/INS centralized Kalman filter include position errors, velocity errors, misalignment angles, the accelerometer and gyro biases, as well as the double-differenced ambiguities ($\Delta\nabla N$), when necessary. The dynamic model for the GPS/INS centralized Kalman filter is given by [3]:

$$\begin{bmatrix} \delta \dot{r}^e \\ \delta \dot{v}^e \\ \dot{\varepsilon}^e \\ \delta \dot{b}^b \\ \delta \dot{d}^b \\ \Delta \nabla \dot{N} \end{bmatrix} = \begin{bmatrix} 0 & I & 0 & 0 & 0 & 0 \\ N^e & -2\Omega_{ie}^e & -F^e & R_b^e & 0 & 0 \\ 0 & 0 & -\Omega_{ie}^e & 0 & R_b^e & 0 \\ 0 & 0 & 0 & -\text{diag}(\alpha_i) & 0 & 0 \\ 0 & 0 & 0 & 0 & -\text{diag}(\beta_i) & 0 \\ 0 & 0 & 0 & 0 & 0 & 0 \end{bmatrix} \cdot \begin{bmatrix} \delta r^e \\ \delta v^e \\ \varepsilon^e \\ \delta b^b \\ \delta d^b \\ \Delta \nabla N \end{bmatrix} + \begin{bmatrix} 0 & 0 & 0 & 0 \\ R_b^e & 0 & 0 & 0 \\ 0 & R_b^e & 0 & 0 \\ 0 & 0 & I & 0 \\ 0 & 0 & 0 & I \\ 0 & 0 & 0 & 0 \end{bmatrix} \cdot \begin{bmatrix} w_f \\ w_w \\ w_b \\ w_d \end{bmatrix} \\ = F_{\text{GPS/INS}} \cdot \delta x + G_{\text{GPS/INS}} \cdot w, \quad (1)$$

where δr^e is the position error vector, δv^e is the velocity error vector, ε^e is the misalignment angle error vector, δb^b is the vector of the accelerometer bias errors, δd^b is the vector of the gyro bias errors, all of aforementioned error states are 3×1 vectors, $\Delta \nabla N$ is the vector of double difference carrier phase ambiguities, w_f is the accelerometers noise, w_w is the

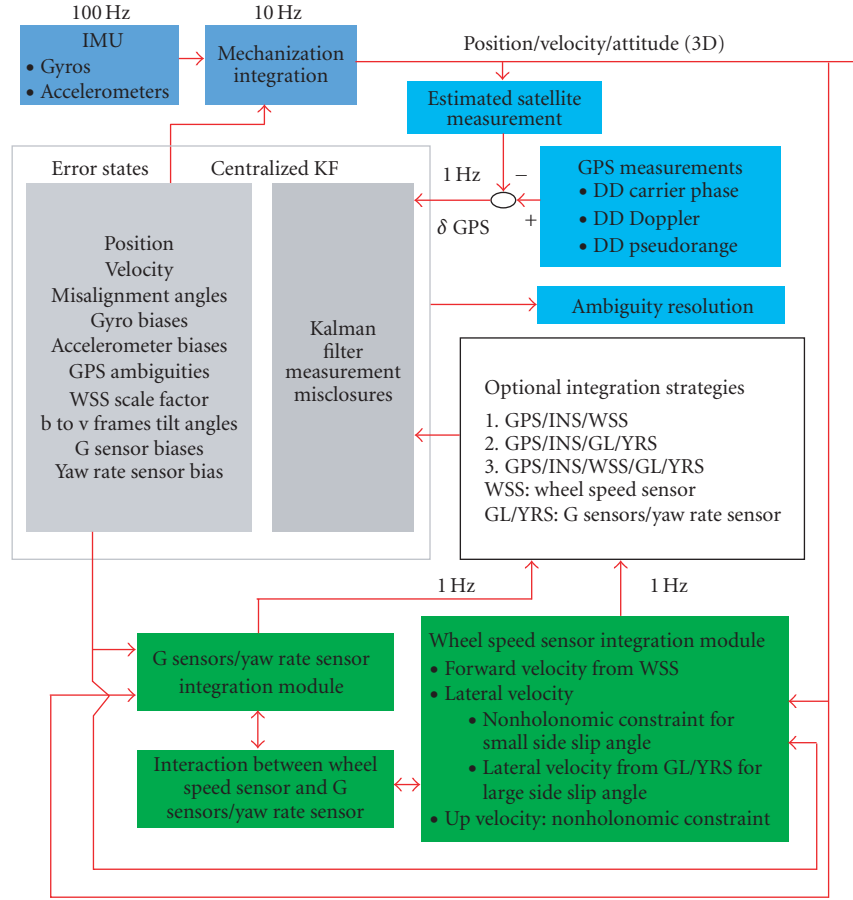


FIGURE 1: Schematics of GPS/low-cost IMU/WSS/GL/YRS integration strategy.

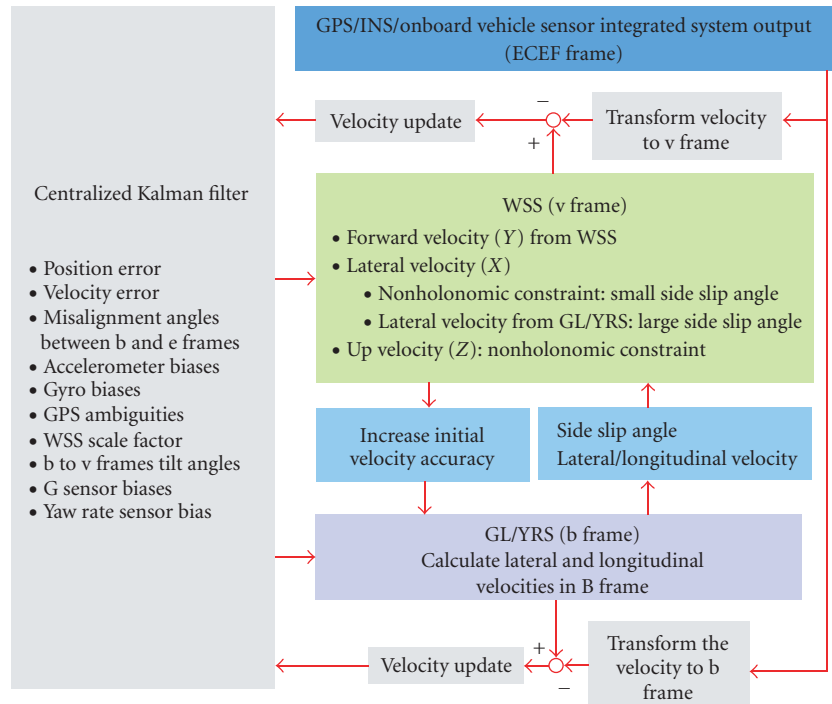


FIGURE 2: The relationship between WSS and GL/YRS.

gyro noise, $\text{diag}(\alpha_i)$ is the diagonal matrix of the time constant reciprocals for the accelerometer bias model, $\text{diag}(\beta_i)$ is the diagonal matrix of the time constant reciprocals for the gyro bias models, w_b is the driving noise for the accelerometer biases, w_d is the driving noise for the gyro biases, R_b^e is the direction cosine matrix between b frame and e frame, F^e is the skew-symmetric matrix of specific force in e frame, N^e is the tensor of the gravity gradients, Ω_{ie}^e is the skew-symmetric matrix of the Earth rotation rate with respect to e frame, δx is the error states vector, and $F_{\text{GPS/INS}}$ is the dynamic matrix for GPS/INS integration strategy, $G_{\text{GPS/INS}}$ is the shaping matrix of the driving noise, and w is the noise matrix.

Equation (1) implies that the bias states for accelerometers and gyros are modeled as first-order Gauss-Markov processes, although any suitable models could be used instead. In terms of the integration strategy shown in Figure 1, the scale factor of WSS and the tilt angle between b and v frames modeled as random constants, as well as the biases of GL/YRS modeled as first-order Gauss-Markov process, are augmented into the error state vector of the centralized Kalman filter to construct the dynamic model, as shown in (2):

$$\begin{bmatrix} \delta \dot{r} \\ \delta \dot{v}^e \\ \dot{\varepsilon}^e \\ \delta \dot{b}^b \\ \delta \dot{d}^b \\ \Delta \nabla \dot{N} \\ \delta \dot{S} \\ \dot{\varepsilon}_{b-v} \\ \delta \dot{b}_{\text{GL}} \\ \delta \dot{d}_{\text{YRS}} \end{bmatrix} = \begin{bmatrix} \text{GPS/INS} & | & \text{O} \\ \hline \begin{matrix} 0 & 0 & 0 & 0 & 0 & 0 \\ 0 & 0 & 0 & 0 & 0 & 0 \\ 0 & 0 & 0 & 0 & 0 & 0 \\ 0 & 0 & 0 & 0 & 0 & 0 \end{matrix} & | & \begin{matrix} 0 & 0 & 0 & 0 \\ 0 & 0 & 0 & 0 \\ 0 & 0 & -\beta_{\text{GL}} & 0 \\ 0 & 0 & 0 & -\beta_{\text{YRS}} \end{matrix} \end{bmatrix} \cdot \begin{bmatrix} \delta r^e \\ \delta v^e \\ \varepsilon^e \\ \delta b^b \\ \delta d^b \\ \Delta \nabla N \\ \delta S \\ \varepsilon_{b-v} \\ \delta b_{\text{GL}} \\ \delta d_{\text{YRS}} \end{bmatrix} + \begin{bmatrix} 0 & 0 & 0 & 0 & 0 & 0 \\ R_b^e & 0 & 0 & 0 & 0 & 0 \\ 0 & R_b^e & 0 & 0 & 0 & 0 \\ 0 & 0 & I & 0 & 0 & 0 \\ 0 & 0 & 0 & I & 0 & 0 \\ 0 & 0 & 0 & 0 & 0 & 0 \\ 0 & 0 & 0 & 0 & 0 & 0 \\ 0 & 0 & 0 & 0 & 0 & 0 \\ 0 & 0 & 0 & 0 & 1 & 0 \\ 0 & 0 & 0 & 0 & 0 & 1 \end{bmatrix} \cdot \begin{bmatrix} w_f \\ w_w \\ w_b \\ w_d \\ w_{\text{GL}} \\ w_{\text{YRS}} \end{bmatrix} \\
 = F_{\text{GPS/INS/WSS/GL/YRS}} \cdot \delta x + G_{\text{GPS/INS/WSS/GL/YRS}} \cdot w, \quad (2)$$

where $F_{\text{GPS/INS/WSS/GL/YRS}}$ is the dynamic matrix for GPS/INS/WSS/GL/YRS integration strategy, $G_{\text{GPS/INS/WSS/GL/YRS}}$ is the shaping matrix, δS is the wheel speed sensor scale factor error state, and $\varepsilon_{b-v} = [\delta\alpha \ \delta\beta \ \delta\gamma]^T$ is the error vector of the tilt angles between the body frame and the vehicle frame corresponding to the X, Y, and Z axes respectively, δb_{GL} is the error vector of the G sensor biases (2×1), δd_{YRS} is the error vector of the yaw rate sensor bias (1×1), β_{GL} (2×1) and β_{YRS} (1×1) are the time constant reciprocals of the first-order Gauss-Markov process model for the GL and YRS biases, respectively, w_{GL} and w_{YRS} are the driving noises for the GL and YRS biases, respectively.

The measurement model in the Kalman filter is generally expressed by (3):

$$z = h(x) + \omega_m, \quad (3)$$

where z is raw measurement, x is estimated state, $h(x)$ is the estimated measurement, and ω_m is the measurement noise.

Most measurement models are nonlinear, and the linearization is needed for the implementation of an extended Kalman filter by (4):

$$z + \left. \frac{\partial z}{\partial x} \right|_{x=x_0} \cdot \delta x = h(x_0) + \left. \frac{\partial h}{\partial x} \right|_{x=x_0} \cdot \delta x + \omega_m, \quad (4)$$

where x_0 is the value of the estimated state, δx is the estimated error state, $\delta z = \left. \frac{\partial z}{\partial x} \right|_{x=x_0} \cdot \delta x$ is the perturbation of the raw measurement, and $\delta h = \left. \frac{\partial h}{\partial x} \right|_{x=x_0} \cdot \delta x$ is the perturbation of the estimated measurement.

By defining the measurement misclosure as (5),

$$W_z = z - h(x_0), \quad (5)$$

equation (4) can be rearranged by (6):

$$\begin{aligned} W_z &= \delta h - \delta z + \omega_m = \left(\left. \frac{\partial h}{\partial x} \right|_{x=x_0} - \left. \frac{\partial z}{\partial x} \right|_{x=x_0} \right) \cdot \delta x + \omega_m \\ &= H \cdot \delta x + \omega_m, \end{aligned} \quad (6)$$

where H is the design matrix.

Since the wheel speed is, by definition, in the vehicle frame and the velocities in the integrated system are parameterized in ECEF frame, the WSS update can be either carried out in the e frame by transforming the WSS measurement into the e frame or carried out in the v frame by transforming the integrated velocities into the v frame. In this research, the WSS update is carried out in the v frame. The velocity in the Y direction of the vehicle frame is given by averaging the two rear wheel speed sensor measurements in (7):

$$v_{\text{WSS}} = \frac{(V_{\text{RL}} + V_{\text{RR}})}{2}, \quad (7)$$

where V_{RR} is the rear right wheel speed sensor measurement, V_{RL} is the rear left wheel speed sensor measurement, and v_{WSS} is the average of the rear wheel speed sensor measurements.

The measurement equation is expressed in (8) with two nonholonomic constraints being applied into the X and Z axes of the vehicle frame:

$$\begin{bmatrix} 0 \\ S \cdot v_{WSS} \\ 0 \end{bmatrix} = R_b^v \cdot (R_b^e)^T \cdot v^e + w_m, \quad (8)$$

where v_{WSS} is the wheel speed sensor measurement given by (7), S is the wheel speed sensor scale factor, and R_b^v is the direction cosine matrix between b and v frames calculated by the following:

$$R_b^v = R_3(\gamma) \cdot R_1(\alpha) \cdot R_2(\beta), \quad (9)$$

where α, β, γ are the tilt angles between the b and v frames with respect to the X, Y , and Z axes, respectively.

The perturbation of the left-hand side of (8) is expressed by (10):

$$\delta \left(\begin{bmatrix} 0 \\ S \cdot v_{WSS} \\ 0 \end{bmatrix} \right) = \begin{bmatrix} 0 \\ v_{WSS} \\ 0 \end{bmatrix} \cdot \delta S = V_{WSS} \cdot \delta S, \quad (10)$$

where $V_{WSS} = [0 \ v_{WSS} \ 0]^T$ is the measurement used for WSS update. It is a 3×1 vector.

The perturbation of right-hand side of (8) is shown in (11):

$$\begin{aligned} \delta(R_b^v \cdot (R_b^e)^T \cdot v^e) \\ = R_b^v \cdot (R_b^e)^T \cdot \delta v^e + R_b^v \cdot (R_b^e)^T \cdot V^E \cdot \varepsilon^e - V^V \cdot \varepsilon_{b-v}, \end{aligned} \quad (11)$$

where v^e is the velocity in the integrated system in e frame, and $v^v = R_b^v \cdot (R_b^e)^T \cdot v^e$ is the integrated velocity in v frame, V^E is the skew-symmetric matrix of the integrated velocity in e frame v^e , and V^V is the skew-symmetric matrix of the integrated velocity expressed in v frame v^v .

From (5) and (8), the measurement misclosure is shown in (12):

$$W_z = \begin{bmatrix} 0 \\ S \cdot v_{WSS} \\ 0 \end{bmatrix} - R_b^v \cdot (R_b^e)^T \cdot v^e. \quad (12)$$

From (6), (10), and (11), the design matrix is derived from (13):

$$\begin{aligned} W_z &= R_b^v \cdot (R_b^e)^T \cdot \delta v^e + R_b^v \cdot (R_b^e)^T \cdot V^E \cdot \varepsilon^e - V^V \cdot \varepsilon_{b-v} \\ &\quad - V_{WSS} \cdot \delta S + w_m = H_{WSS} \cdot \delta x + w_m. \end{aligned} \quad (13)$$

Thus, the design matrix H_{WSS} is summarized by (14):

$$\begin{aligned} H_{WSS} &= [O_{3 \times 3} \quad Q \quad Q' \quad O_{3 \times 3} \quad O_{3 \times 3} \quad O_{3 \times AR} \quad -V_{WSS} \quad -V^V \quad O_{3 \times 2} \quad O_{3 \times 1}], \\ &\quad \text{where } Q = R_b^v \cdot (R_b^e)^T, \quad Q' = R_b^v \cdot (R_b^e)^T \cdot V^E. \end{aligned} \quad (14)$$

Equation (14) is a hyper matrix with each submatrix corresponding to the error states defined in (2). O is a zero matrix with the subscripted dimensions and AR is the number of float ambiguities and is equal to zero when all the ambiguities are fixed.

When using the G sensors and yaw rate sensor, the equation of motion in the body frame is shown in (15) [12, 13]. Since the nonholonomic constraint is applied in the vertical direction, the vertical velocity is only coupled with gravity,

$$\begin{aligned} \dot{V}_x^b &= (f_x - b_{GL1}) - V_y \cdot (r - d_{YRS}) + g_x^b, \\ \dot{V}_y^b &= (f_y - b_{GL2}) + V_x \cdot (r - d_{YRS}) + g_y^b, \\ \dot{V}_z^b &= g_z^b, \end{aligned} \quad (15)$$

where f_x and f_y are the specific force measurements from the G sensors, γ is the yaw rate measurement, V_x^b, V_y^b, V_z^b are the velocities in the b frame, and g_x^b, g_y^b, g_z^b are the gravity elements in the b frame, $b_{GL} = [b_{GL1} \ b_{GL2} \ 0]^T$ and d_{YRS} are the biases of G sensors and yaw rate sensor, respectively.

The gravity vector in (15) is derived from the gravity vector in the e frame by (16):

$$g^b = (R_b^e)^T \cdot g^e, \quad (16)$$

where g^e and g^b are the gravity vector in e and b frame, respectively.

By defining

$$M = \begin{bmatrix} 1 & 0 & 0 \\ 0 & 1 & 0 \\ 0 & 0 & 0 \end{bmatrix}, \quad f = \begin{bmatrix} f_x \\ f_y \\ 0 \end{bmatrix}, \quad J = \begin{bmatrix} 0 & -1 & 0 \\ 1 & 0 & 0 \\ 0 & 0 & 0 \end{bmatrix}, \quad (17)$$

equation (15) can be replaced by the state space vector in (18), which simplifies the mathematical analysis

$$\dot{V}^b = M \cdot (f - b_{GL}) + J \cdot V^b \cdot (\gamma - d_{YRS}) + g^b, \quad (18)$$

where V^b is the velocity vector in the b frame.

Using the trapezoid method [15], the velocity in the body frame can be integrated from (19) as

$$\begin{aligned} V^b &= V_0^b + \frac{1}{2} (k_1 + k_2) \cdot \Delta t, \\ k_1 &= M \cdot (f_{(0)} - b_{GL(0)}) + J \cdot V_0^b (\gamma_{(0)} - d_{YRS(0)}) + g_0^b, \\ k_2 &= M \cdot (f - b_{GL}) + J \cdot (V_0^b + k_1 \cdot \Delta t) \cdot (\gamma - d_{YRS}) + g^b, \end{aligned} \quad (19)$$

where V_0^b is the initial velocity that comes from the integrated system, $f_{(0)}$ and $\gamma_{(0)}$ are the G sensors and yaw rate sensor measurements at last epoch, $b_{GL(0)}$ and $d_{YRS(0)}$ are the G sensors and yaw rate sensor biases at last epoch, g_0^b is last epoch's gravity vector in the b frame, k_1 and k_2 are parameters for the trapezoid integration, Δt is the integration time interval (defined to be 1 second in this research).

To conduct the GL/YRS update in the b frame, the velocity in the integrated system is transformed from the e frame

into the b frame, and the measurement equation is expressed by (20):

$$V^b = (R_b^e)^T \cdot v^e, \quad (20)$$

where V^b is the velocity computed from (19), and v^e is the velocity of the integrated system in the e frame.

The perturbation of the gravity vector in (16) can be derived as shown in (21):

$$\delta g^b = (R_b^e)^T \cdot N^e \cdot \delta r^e + (R_b^e)^T \cdot G^e \cdot \varepsilon^e, \quad (21)$$

where N^e is the tensor of the gravity gradients, G^e is the skew-symmetric matrix of the gravity vector in the e frame.

Using (19) and (21), the perturbation of the velocity vector V^b is expressed by (22):

$$\begin{aligned} \delta V^b &= \frac{1}{2}(\delta k_1 + \delta k_2) \cdot \Delta t \\ &= \frac{\Delta t}{2}(R_b^e)^T \cdot N^e \cdot \delta r^e + \frac{\Delta t}{2}(R_b^e)^T \cdot G^e \cdot \varepsilon^e \\ &\quad + \frac{\Delta t}{2}M \cdot \delta b_{GL} + \frac{\Delta t}{2}J \cdot (V_0^b + k_1 \cdot \Delta t) \cdot \delta d_{YRS}. \end{aligned} \quad (22)$$

The perturbations of the right-hand side of (20) are shown in (23):

$$\delta((R_b^e)^T \cdot v^e) = (R_b^e)^T \cdot \delta v^e + (R_b^e)^T \cdot V^E \cdot \varepsilon^e, \quad (23)$$

where V^E is the skew-symmetric matrix of the integrated velocity in the e frame.

Similarly to WSS update, the measurement misclosure can be derived from (5) and (20) as shown in (24):

$$W_z = V^b - (R_b^e)^T \cdot v^e. \quad (24)$$

Based on (22) and (23), the design matrix related to the GL/YRS velocity update is consequently derived in (25) in terms of (6):

$$\begin{aligned} W_z &= \delta((R_b^e)^T \cdot v^e) - \delta V^b + w_m \\ &= -\frac{\Delta t}{2} \cdot (R_b^e)^T \cdot N^e \cdot \delta r^e + (R_b^e)^T \cdot \delta v^e \\ &\quad + \left[(R_b^e)^T \cdot V^E - \frac{\Delta t}{2} \cdot (R_b^e)^T \cdot G^e \cdot \Delta t \right] \varepsilon^e \\ &\quad - \frac{\Delta t}{2} \cdot M \cdot \delta b_{GL} - \frac{\Delta t}{2} \cdot J \cdot (V_0^b + k_1 \cdot \Delta t) \\ &\quad \cdot \delta d_{YRS} + w_m = H_{GL/YRS} \cdot \delta x + w, \end{aligned} \quad (25)$$

where $H_{GL/YRS}$ is the design matrix for the GL/YRS update, which is coupled with the error states of position, velocity, b-to-e frame misalignment angles, and GL/YRS biases. More specifically, the design matrix is

$$H_{GL/YRS} = \begin{bmatrix} U & (R_b^e)^T & U' & O_{3 \times 3} & O_{3 \times 3} & O_{3 \times AR} & O_{3 \times 1} & O_{3 \times 3} & -\frac{\Delta t}{2}M & U'' \end{bmatrix},$$

$$\text{where } U = -\frac{\Delta t}{2}(R_b^e)^T N^e, \quad U' = (R_b^e)^T V^E - \frac{\Delta t}{2}(R_b^e)^T \cdot G^e \Delta t,$$

$$U'' = -\frac{\Delta t}{2}J(V_0^b + k_1 \cdot \Delta t). \quad (26)$$

In this research, the noise power of GL/YRS was determined from a static test by calculating the average standard deviation across 40 evenly spaced 1-second intervals of the static data. When performing integration with the GL/YRS measurements to derive the velocity, the noise in GL/YRS behaves as random walk error because of the integration. The propagation of G sensor noise on the velocity from the trapezoid integration is correlated with the integration time length, that is,

$$\sigma_{V_{Noise}^b}^2 = \sigma_f^2 \cdot \Delta t, \quad (27)$$

where σ_f^2 is the noise power of G sensors, Δt is the time interval for the integration, and $\sigma_{V_{Noise}^b}^2$ is the variance propagated by the measurement noise.

Considering the integration is performed every 1 second and the initial value comes from the integrated system every 1 second, $\sigma_{V_{Noise}^b}^2 = \sigma_f^2$ herein. Therefore, the velocity variance for the GL/YRS velocity update can be tuned adaptively in terms of variance propagation theory from (19), which is shown in (28),

$$\begin{aligned} \sigma_{V^b}^2 &= \sigma_{V_0^b}^2 + \frac{1}{4} \cdot (\sigma_{k1}^2 + \sigma_{k2}^2) \cdot \Delta t^2, \\ \sigma_{g^b}^2 &= (R_b^e)^T \cdot N^e \cdot \sigma_{re}^2 \cdot (N^e)^T \cdot R_b^e, \\ \sigma_{k1}^2 &= M(\sigma_f^2 + \sigma_{b_{GL(0)}}^2) \cdot M^T + J\sigma_{V_0^b}^2 \cdot (\gamma_{(0)} - d_{YRS(0)})^2 \cdot J^T, \\ &\quad + J \cdot V_0^b \cdot (\sigma_y^2 + \sigma_{d_{YRS(0)}}^2) \cdot (J \cdot V_0^b)^T + \sigma_{g^b}^2, \\ \sigma_{k2}^2 &= M(\sigma_f^2 + \sigma_{b_{GL}}^2) \cdot M^T + J \cdot (\sigma_{V_0^b}^2 + \sigma_{k1}^2 \cdot \Delta t^2) \\ &\quad \cdot (\gamma - d_{YRS})^2 \cdot J^T + J \cdot (V_0^b + k_1 \cdot \Delta t) \cdot (\sigma_y^2 + \sigma_{d_{YRS}}^2) \\ &\quad \cdot (V_0^b + k_1 \cdot \Delta t)^T \cdot J^T + \sigma_{g^b}^2, \end{aligned} \quad (28)$$

where $\sigma_{V^b}^2$ is the velocity variance of the GL/YRS, $\sigma_{b_{GL}}^2$ and $\sigma_{d_{YRS}}^2$ are the estimated variances of the GL/YRS biases provided by the Kalman filter, $\sigma_{b_{GL(0)}}^2$ and $\sigma_{d_{YRS(0)}}^2$ are the variances of GL/YRS biases at the previous step, $\sigma_{V_0^b}^2$ is the initial velocity variance from the integrated system, $\sigma_{g^b}^2$ is the variance of the gravity vector in the body frame, σ_{re}^2 is the position variance in e frame.

Figure 3 describes the geometric relationship between the WSS and GL/YRS, as well a simplified vehicle's bicycle model that contains the rear wheel side slip angle. The rear wheel side slip angle can be calculated in (29) from the transformed velocity in the lateral and longitudinal directions using [18]:

$$\beta_r = \tan^{-1} \left[\frac{V_x^b - L_r \cdot \gamma}{V_y^b} \right], \quad (29)$$

where β_r is the rear wheel side slip angle, L_r is the distance between the GL/YRS and WSS, and V_x^b and V_y^b are the lateral and longitudinal velocity derived from the GL/YRS.

The lateral nonholonomic constraint is most frequently violated when the side slip angle is large. Therefore, the side

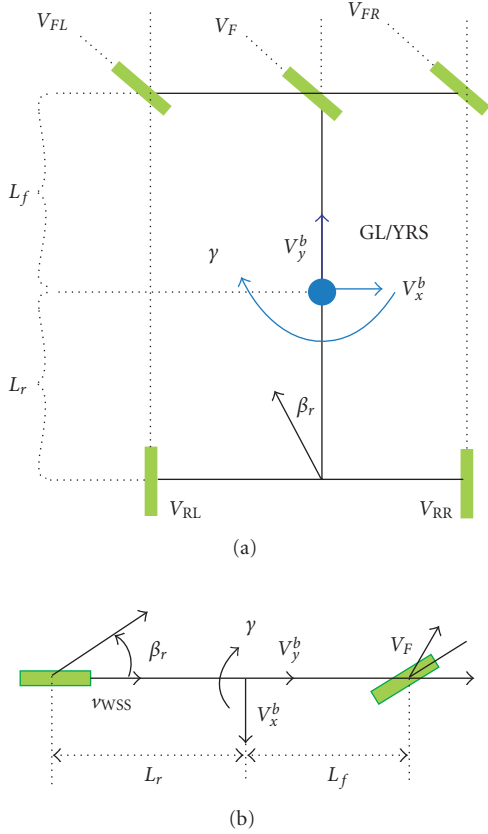


FIGURE 3: The geometric relationship between WSS, GL/YRS, and the side slip angle.

slip angle provides a way to detect and alleviate the violation of the lateral nonholonomic constraint. This mechanism is designed as described below.

When the side slip angle is smaller than a threshold (5 degrees in this research), it means that the nonholonomic constraint is valid, and the nonholonomic constraints are applied in both the lateral and vertical directions. In this case, (30) is used as the measurement for WSS update:

$$V_{WSS} = \begin{bmatrix} 0 \\ v_{WSS} \\ 0 \end{bmatrix}. \quad (30)$$

By contrast, if the side slip angle exceeds a threshold, the violation of the lateral nonholonomic constraint can be replaced by the GL/YRS derived lateral velocity, that is,

$$V_{WSS} = \begin{bmatrix} V_y^b \\ v_{WSS} \\ 0 \end{bmatrix}. \quad (31)$$

The longitudinal element is a real value that comes from WSS. The lateral and vertical elements are virtual values that can be either nonholonomic constraints or other values from external measurements. Despite the fact that a lateral velocity can also be given from the INS mechanization output,

it cannot be employed as an external or independent measurement to remove the lateral constraint if violated. Otherwise, a correlation or dependence will be introduced when performing external update to the centralized Kalman filter. GL/YRS unit, however, provides redundant and independent measurement for detecting and alleviating the violation of the lateral constraint.

To achieve a high positioning accuracy, it is necessary to switch (30) and (31) in terms of a side slip angle threshold. With a small side slip angle, the lateral constraint is more close to the real situation where the lateral velocity is very small. If (31) is still being used when the lateral constraint is not violated; the error and noise from GL/YRS unit will degrade the positioning accuracy.

During GPS outages, the absolute velocity update from WSS limits the longitudinal velocity drift error and increases the accuracy of initial longitudinal velocity for GL/YRS. Alternatively, GL/YRS unit provides a way to detect and alleviate the violation of the lateral nonholonomic constraint on WSS. This kind of effective cooperation between WSS and GL/YRS can adapt to a variety of driving cases with a high positioning accuracy during GPS outages.

5. TESTS, RESULTS, AND ANALYSIS

To investigate the benefits gained from onboard vehicle sensors, two tests were conducted in an open sky and processed in post-mission and in a suburban area in real time. In this section, the data processing and analysis method is illustrated first. The tests are then described and the results are analyzed, respectively, for each test.

5.1. Data processing and analysis method

The data collected (see Sections 5.2 and 5.3) were processed and the results are analyzed in the following way. First, the satellite DOP (horizontal and vertical dilution of precision), the GPS availability as well as the number of resolved ambiguities are given. In the GPS/low-cost IMU/onboard vehicle sensor integrated system, GPS is the driving factor in terms of system accuracy. When GPS is fully available, GPS plays a dominant role in the integrated system and determines the absolute accuracy of the integrated system. To this end, the GPS availability, namely, the satellite availability in both the base and remote stations is analyzed in all the tests. Also, the satellite DOP which is a measure of the satellite geometry is also shown in each test. Lower DOP values give better position accuracy. The correct and fast ambiguity resolution has crucial effects on the positioning accuracy when the carrier phase measurement is used. In general, correct ambiguity resolution can result in the centimetre-level accuracy. Associated with the numbers of satellites tracked, the number of double difference ambiguities that have been fixed is shown. Second, a reference solution is generated from another independent system such as the GPS/HG1700 IMU (tactical grade) integrated system or GPS/CIMU (navigation grade) system. It is important to know the accuracy of the reference solution. Furthermore, the reference solution

can be generated by either the optimal backward smoothing technique or by a forward Kalman filtering technique. Both the GPS/HG1700 IMU and GPS/CIMU integrated solutions are accurate to the centimetre level, and there is no significant difference in the optimal smoothing and the forward Kalman filtering solutions when GPS availability is good. Therefore, the reference solution in the post-mission open-sky kinematic test was generated by the GPS/HG1700 IMU integrated solution without backward smoothing. However, in the suburban real-time test, both tactical and navigation grade IMUs are susceptible to position and velocity drift due to the frequent masking of satellite signals by trees, buildings, and underpasses. As the CIMU is more accurate than the HG1700 IMU, the reference trajectory was generated by the GPS/CIMU with an optimal backward smoothing technique because it will be more reliable than that generated by the GPS/HG1700 IMU. For the reference generated by GPS/HG1700 solution, its accuracy is shown by the estimated standard deviations of the position. The GPS/CIMU reference solution processed by the Applanix POS Pac software gives the estimated RMS error of the estimated position. The estimated RMS errors are equivalent to the estimated standard deviation assuming the estimated error has zero mean. Third, the performances of four integration strategies are assessed with respect to the reference solution. The integration strategies include GPS/INS without the aiding from the onboard vehicle sensors, GPS/INS/WSS with the non-holonomic constraints applied in the lateral and the vertical directions, and GPS/INS/GL/YRS as well as a combined integration strategy using GPS/INS/WSS/GL/YRS with a detection and alleviation mechanism for the lateral nonholonomic constraint violation.

As the side slip angle is a key parameter for the side slip detection, the side slip angles will be given in the following analysis.

5.2. Post-mission test in open-sky area

The onboard vehicle sensor and the low-cost IMU data were collected and logged onto a desktop PC through a serial port at 100 Hz. The GPS base station was set up on a pillar with a surveyed coordinate. For the open-sky kinematic test in post-mission, the GPS base station data was saved onto a flash card. The GPS/HG1700 IMU (tactical grade IMU) integrated solution generated the reference solution. The HG1700 IMU data were time tagged and logged by a NovAtel SPAN system at 100 Hz.

The purpose of the post-mission open-sky kinematic test was to tune the Kalman filter, assess the modeling of sensors and the validity of the integration algorithm, and to assess the performance and positioning accuracy for various integration strategies by simulating GPS outages. Figure 4 gives an overview of the open-sky test that was conducted on March 21, 2006 in Springbank near Calgary, which is an open-sky area with good GPS satellite visibility. The system was run for 10 minutes in static mode for initialization, and approximately for 30 minutes in kinematic mode for positioning and navigation testing with a maximum baseline

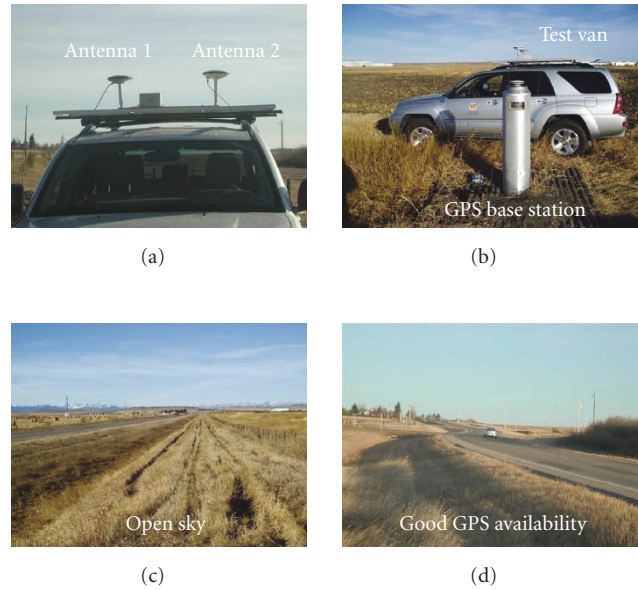


FIGURE 4: Open-sky test that processed in post-mission.

length of 4 km. Due to a benign environment for the ambiguity resolution, the GPS measurements used in this test include L1 carrier phase, Doppler and the C/A code.

In the open-sky test, 12 GPS outages were simulated and the horizontal position RMS drift error with respect to the reference solution was computed. Also, the actual position difference and the estimated position standard deviations in the Kalman filter were compared. The estimated standard deviation should have good agreement with the statistics of the actual position difference in an ideal case. In practice, this indicates that the model and parameters in the Kalman filter are well tuned if the estimated standard deviation does not deviate too much from the statistics of the actual position difference.

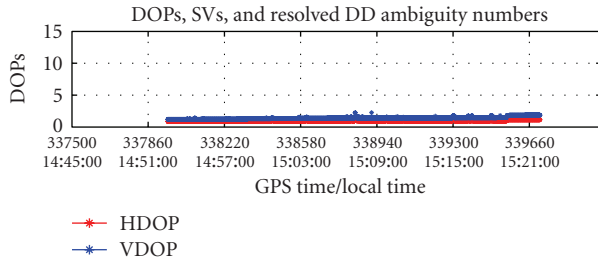
Figure 5 shows the satellite DOP values, the number of tracked satellites at the base and remote stations (and their difference), and the number of fixed ambiguities. It can be seen that the open-sky test had good GPS availability and satellite geometry, as well as sufficient double difference (DD) ambiguities resolved.

In the open-sky area, the accuracy of the reference solution generated by GPS/HG1700 IMU integrated system is dominated by GPS. As shown in Figure 6, the carrier phase residual is around 2-3 centimetres and the C/A code residual is unbiased. It is reasonable to conclude that GPS ambiguity is correctly resolved. Hence the reference solution is accurate to be at centimetre level.

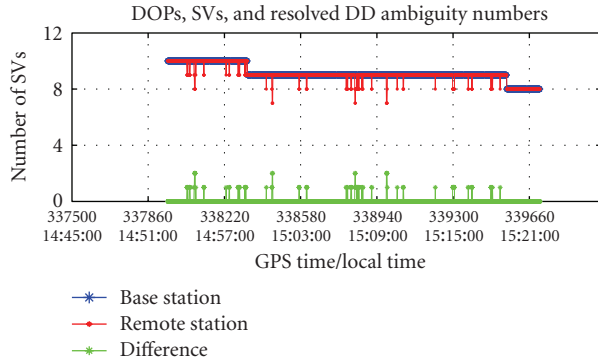
To investigate the benefits gained from the integration of the onboard vehicle sensors, 12 GPS outages of 40-second duration were simulated. The simulated GPS outages cover a wide range of vehicle dynamics. The side slip angles (by labeling the simulated GPS outage number and by zooming the side slip angles of five simulated GPS outages) are shown in Figure 7. As the open-sky test was conducted in

TABLE 1: Horizontal position RMS error and the average estimated standard deviation at the end of 40-second GPS outages for the open-sky test that is processed in post-mission.

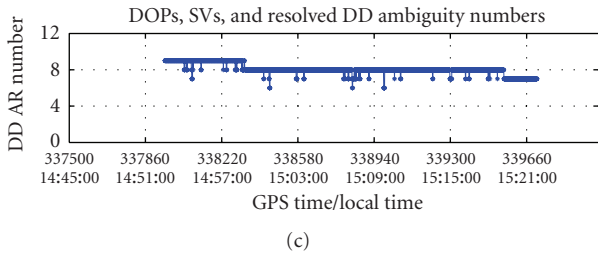
Strategies	Horizontal position RMS error and average estimated standard deviation at the end of 40-second GPS outages	
	Horizontal position RMS error [m]	Average estimated standard deviation [m]
GPS/INS	30.48	31.98
GPS/INS/GL/YRS	25.00	24.90
GPS/INS/WSS	2.92	3.59
GPS/INS/WSS/GL/YRS	2.26	2.02



(a)



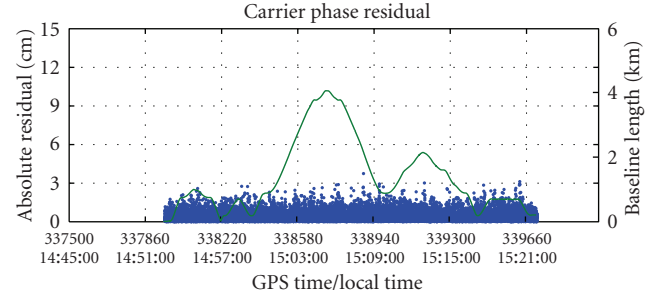
(b)



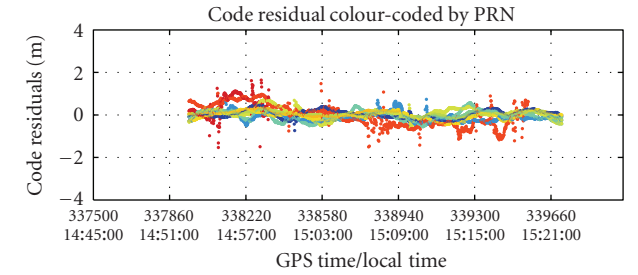
(c)

FIGURE 5: Satellite DOPs, satellite numbers, and the resolved ambiguities in the open-sky test that processed in post-mission.

March at Springbank near Calgary, the icy and bumpy road contributed to the maximum side slip angle at 20 degrees. Figure 8 compares the RMS horizontal position error and the average estimated standard deviation during the 40-second GPS outages with respect to the four proposed integration strategies. The RMS horizontal position error and the average estimated standard deviation are summarized in Table 1.



(a)



(b)

FIGURE 6: Residuals of carrier phase and C/A code and the baseline length for open-sky test that processed in post-mission.

During GPS outages and without any external aiding from the onboard vehicle sensors, the low-cost IMU drifts very rapidly. However, significant benefits can be gained from the integration of the wheel speed sensor with improvements in the horizontal positioning accuracy of 90.4%. The improvement gained from the integration GL/YRS is less significant than WSS due to the low quality of GL/YRS unit. However, when the WSS and GL/YRS are incorporated (GPS/INS/WSS/GL/YRS strategy) to detect and alleviate the violation of the lateral nonholonomic constraint, the horizontal positioning accuracy can be improved by 92.6%, which is correlated with the degree of the side slip. Due to the well-tuned Kalman filter, the actual horizontal position errors and the average estimated standard deviations in the Kalman filter have good agreement for all integration strategies.

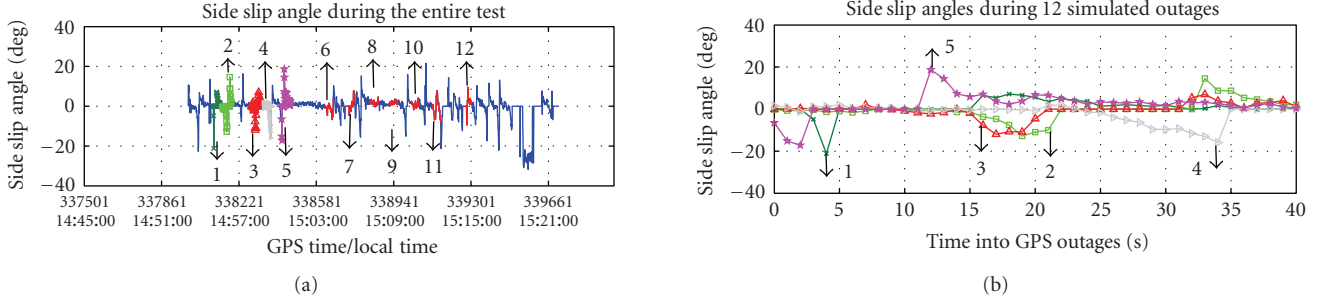


FIGURE 7: Side slip angles in the open-sky test that processed in post-mission.

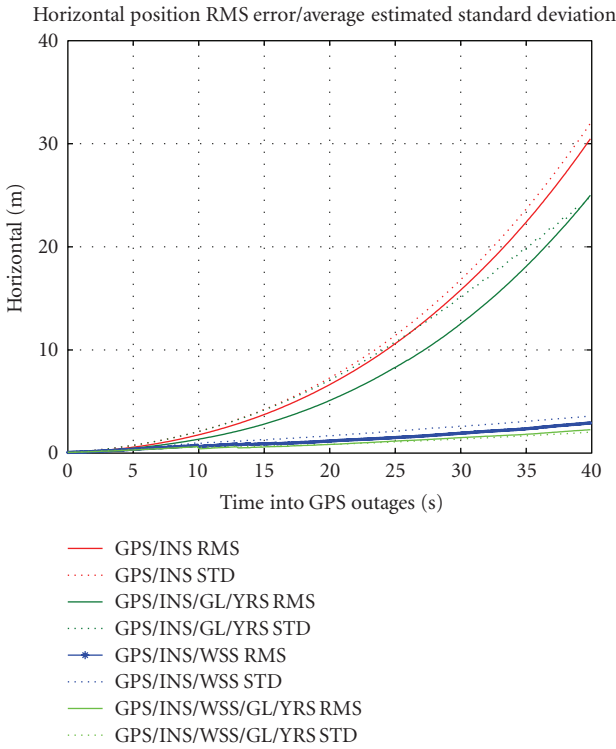


FIGURE 8: Horizontal position RMS error and average estimated standard deviation during 12 simulated GPS outages for the open-sky test that processed in post-mission.

5.3. Real-time test in suburban area

For real-time test in suburban area, the GPS base station data was broadcast to the remote station via a pair of FreeWave radio link antennas and transceivers. The reference solution was generated by a GPS/CIMU (navigational grade IMU) integrated solution. The CIMU data were collected at 200 Hz by an Applanix POS LS system.

The real-time tests gave an evaluation of the validity of the design of the Kalman filter as well as the impact of various sensor combinations when the satellite signals were masked. The real-time test in suburban area test started and ended in front of the Calgary Centre for Innovative Technology

TABLE 2: Horizontal position difference RMS for the real-time suburban area test.

Strategies	Horizontal position difference RMS [m]
GPS/INS	1.09
GPS/INS/GL/YRS	1.05
GPS/INS/WSS	0.48
GPS/INS/WSS/GL/YRS	0.38

(CCIT) building at the University of Calgary on June 28, 2006. The test was conducted around the campus with a maximum baseline of 2.5 km, and 8 minutes of static mode for the initialization, as well as approximately 20 minutes for the kinematic part. As shown in Figure 9, the GPS base station and radio link antennas were set up on the roof of the CCIT building. Also, partial and complete GPS outages were mainly introduced by the dense foliage, small buildings near the street as well as bridges. Unlike the open-sky area, the multipath error significantly increases in suburban area. To guarantee reliable ambiguity resolution, the widelane carrier phase (rather than L1 in the open-sky test), Doppler and the C/A code measurements were used. The use of widelane measurements is at the cost of amplifying the noise by the linear combination of the L1 and L2 carrier phases. However, it is a tradeoff between fast and reliable ambiguity resolution and an increase in the noise.

For the real-time suburban area test, DOP values, the number of tracked satellites at the base and remote stations (and their difference), and the number of fixed ambiguities are shown in Figure 10. Most of the horizontal DOP are less than two with several cases exceeding five. However, the GPS availability is far from ideal since dense foliage, underpasses, and the buildings near the road introduced partial and complete satellite masking. The difference in the number of satellites tracked between the GPS base and the remote stations indicate the level of signal masking.

Figure 11 illustrates the estimated position accuracies for the reference solution used for the real-time test. It indicates that the estimated accuracy of the GPS/CIMU with optimal backward smoothing is closely related to the GPS availability. When GPS is fully available, the estimated accuracy is comparable to that in the open sky. However, the estimated



(a)



(b)



(c)

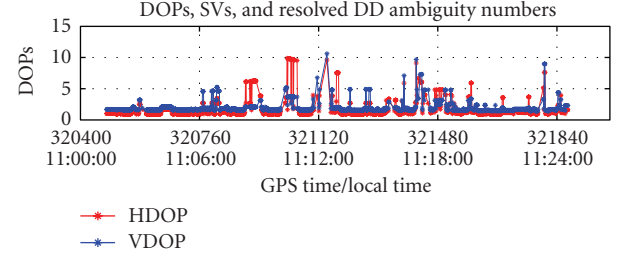


(d)

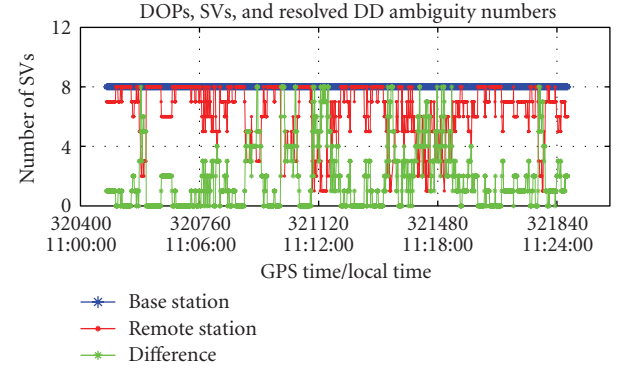
FIGURE 9: Real-time test in suburban area.

accuracy is susceptible to the masking of the satellites as well as the durations of the masking. The longer the duration of GPS blockage, the lower the estimated accuracy. Nevertheless, due to the superior quality of the navigational grade CIMU, the worst case for the estimated accuracy, which is relevant to the masking of GPS signal, is at the decimetre level (10–15 cm) for this test. Its accuracy is much higher than for the low-cost IMU, and thus serves as a good reference solution.

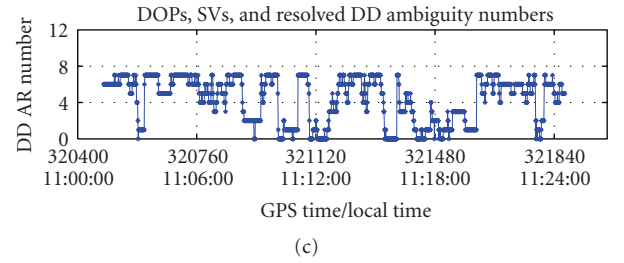
Figure 12 shows the side slip angle during the entire real-time test. As the test was conducted in the summer time on a relatively flat road, the maximum side slip angle was less than 10 degrees, with maximum values being sparsely distributed around the specific epochs at 321100 seconds, 321400 seconds, and 321840 seconds, respectively.



(a)



(b)



(c)

FIGURE 10: The satellite DOPs, satellite numbers, and the resolved ambiguities in the real-time suburban area test.

The horizontal position computed from the four integration strategies is compared with the reference solution, as shown in Figure 13. When GPS is fully available, GPS determines the absolute accuracy of the integrated system, and the horizontal position difference for each integration strategy is very small. During GPS outages, the horizontal position difference increases significantly depending on the duration of the outages. By comparing the four integration strategies, the aiding from the WSS can be seen to significantly reduce the position drift as compared to the stand-alone low-cost IMU. The benefits gained from GPS/INS/GL/YRS integration strategy is somewhat limited. However, the horizontal positioning accuracy can be further improved by the GPS/INS/WSS/GL/YRS integration strategy with respect to GPS/INS/WSS integration strategy if a large side slip occurs. This fact can be verified in Figure 13 around the specific epochs at 321100 seconds, 321400 seconds, and 321840 seconds, which are relevant to the large side slip angles. For easy comparisons, Table 2 statistically summarizes the horizontal

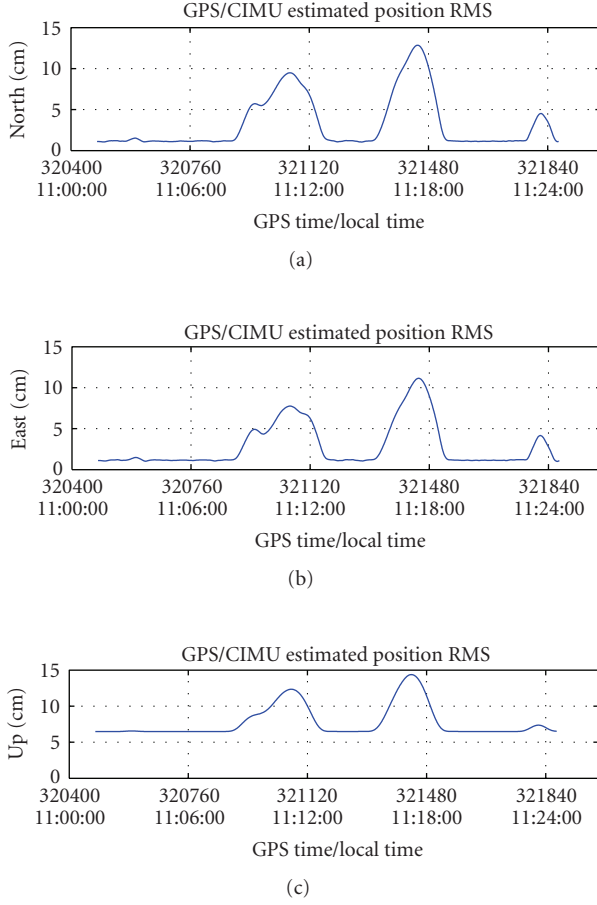


FIGURE 11: The position accuracy for the reference solution generated by GPS/CIMU integrated system for the real-time suburban area test.

RMS position difference for the four integration strategies. The benefits gained from the integration of the onboard vehicle sensors on the positioning accuracy can be seen clearly.

6. CONCLUSIONS

In this paper, GPS, a low-cost IMU and several onboard vehicle sensors (four wheel speed sensors, two G sensors, and a yaw rate sensor) are integrated using a closed loop centralized Kalman filter. The integration strategies and the integration algorithms were developed. A mechanism was proposed for detecting and alleviating the violation of the lateral non-holonomic constraint on the wheel speed sensor.

It is consistently illustrated by all the tests that GPS plays a dominant role in determining the absolute positioning accuracy of the system when GPS is fully available. The integration of onboard vehicle sensors can enhance the horizontal positioning accuracy during GPS outages.

The improvements from the wheel speed sensor over GPS and low-cost IMU integrated system are 90.4% for the open-sky test (post-mission processing with 12 simulated GPS out-

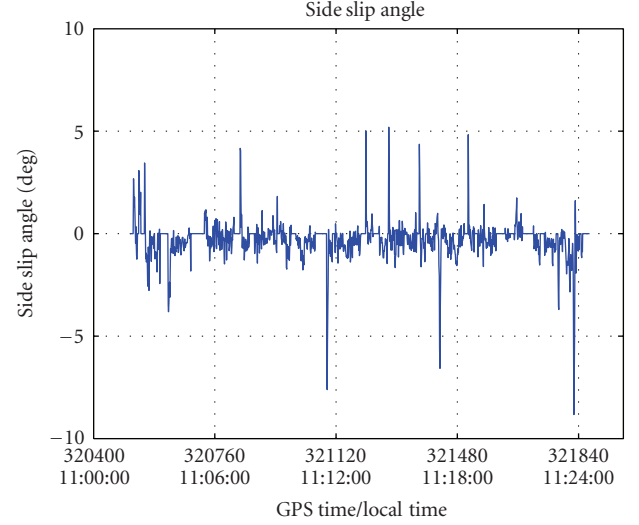


FIGURE 12: Side slip angle for the real-time suburban area test.

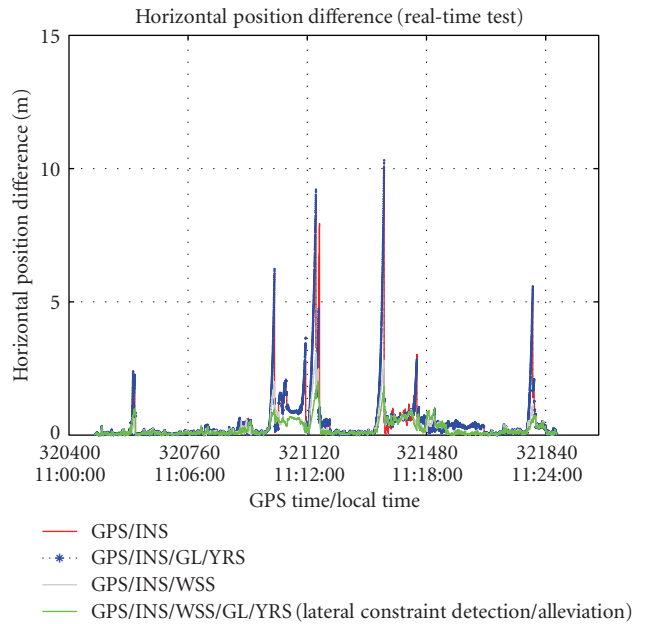


FIGURE 13: Horizontal position difference between GPS/INS/on-board vehicle sensor integrated output and the reference solution for the real-time suburban area test.

ages) and 56.0% for suburban area real-time test, respectively.

The improvement from automotive grade GL/YRS unit is less significant than the wheel speed sensor. It is only 18.0% for the open-sky test and 3.7% for suburban area real-time test, respectively. However, the strategy that integrates all sensors to detect and alleviate the violation of the lateral non-holonomic constraints performs best. Percentage improvements on horizontal positioning accuracy reached 92.6% for open-sky test and 65.1% for the suburban area real-time test.

REFERENCES

- [1] H. E. Tseng, B. Ashrafi, D. Madau, T. A. Brown, and D. Recker, "The development of vehicle stability control at Ford," *IEEE/ASME Transactions on Mechatronics*, vol. 4, no. 3, pp. 223–234, 1999.
- [2] D. M. Bevly, A. Rekow, and B. Parkinson, "Evaluation of a blended dead reckoning and carrier phase differential GPS system for control of an off-road vehicle," in *Proceedings of the 12th International Technical Meeting of the Satellite Division of the Institute of Navigation (ION GPS '99)*, pp. 2061–2069, Sashville, Tenn, USA, September 1999.
- [3] M. G. Petovello, "Real-time integration of tactical grade IMU and GPS for high-accuracy positioning and navigation," Ph.D. thesis, UCGE Report 20173, Department of Geomatics Engineering, University of Calgary, Calgary, Canada, 2003.
- [4] S. Sukkarieh, *Low cost, high integrity, aided inertial navigation systems for autonomous land vehicles*, Ph.D. thesis, Australian Center for Field Robotics, University of Sydney, Sydney, Australia, 2000.
- [5] S. Godha, "Performance evaluation of low cost MEMS-based IMU integrated with GPS for land vehicle navigation application," M.Sc. thesis, UCGE Report #20239, Department of Geomatics Engineering, University of Calgary, Calgary, Canada, 2006.
- [6] R. S. Harvey, "Development of a precision pointing system using an integrated multi-sensor approach," M.Sc. thesis, UCGE Report 20117, Department of Geomatics Engineering, University of Calgary, Calgary, Canada, 1998.
- [7] J. Stephen, "Development of a multi-sensor GNSS based vehicle navigation system," M.Sc. thesis, UCGE Report 20140, Department of Geomatics Engineering, University of Calgary, Calgary, Canada, 2000.
- [8] C. Hay, "Turn, turn, turn wheel-speed dead reckoning for vehicle navigation," *GPS World*, vol. 16, no. 10, pp. 37–42, 2005.
- [9] Ph. Bonnifait, P. Bouron, D. Meizel, and P. Crubillé, "Dynamic localization of car-like vehicles using data fusion of redundant ABS sensors," *Journal of Navigation*, vol. 56, no. 3, pp. 429–441, 2003.
- [10] J. Kubo, T. Kindo, A. Ito, and S. Sugimoto, "DGPS/INS/wheel sensor integration for high accuracy land-vehicle positioning," in *Proceedings of the 12th International Technical Meeting of the Satellite Division of the Institute of Navigation (ION GPS '99)*, pp. 555–564, Nashville, Tenn, USA, September 1999.
- [11] J. Gao, M. G. Petovello, and M. E. Cannon, "Development of precise GPS/INS/wheel speed sensor/yaw rate sensor integrated system," in *Proceedings of the National Technical Meeting of the Institute of Navigation (ION NTM '06)*, pp. 780–792, Monterey, Calif, USA, January 2006.
- [12] A. Brandit and J. F. Gardner, "Constrained navigation algorithms for strapdown inertial navigation systems with reduced set of sensors," in *Proceedings of the American Control Conference*, vol. 3, pp. 1848–1852, Philadelphia, Pa, USA, June 1998.
- [13] G. Dissanayake, S. Sukkarieh, E. Nebot, and H. DurrantWhyte, "The aiding of a low cost strapdown inertial measurement unit using vehicle model constraints for land vehicle applications," *IEEE Transactions on Robotics and Automation*, vol. 17, no. 5, pp. 731–747, 2001.
- [14] R. Anderson and D. M. Bevly, "Estimation of slip angles using a model based estimator and GPS," in *Proceedings of the American Control Conference*, vol. 3, pp. 2122–2127, Boston, Mass, USA, June-July 2004.
- [15] C. Jekli, *Inertial Navigation Systems with Geodetic Applications*, Walter de Gruyter, New York, NY, USA, 2000.
- [16] R. G. Brown and P. Y. C. Hwang, *Introduction to Random Signals and Applied Kalman Filtering*, John Wiley & Sons, New York, NY, USA, 2nd edition, 1992.
- [17] P. J. G. Teunissen and A. Kleusberg, *GPS for Geodesy*, Springer, New York, NY, USA, 1996.
- [18] L. R. Ray, "Nonlinear state and tire force estimation for advanced vehicle control," *IEEE Transactions on Control Systems Technology*, vol. 3, no. 1, pp. 117–124, 1995.